The Nucleon Axial-Vector Form Factor at the Physical Point with the HISQ Ensembles

A. Bazavov,[1] C. DeTar,[2] A. X. El-Khadra,[3,4] E. Gámiz,[5] Steven Gottlieb,[6] U. M. Heller,[7] R. J. Hill,[8,4] C. Hughes,[4,*] W. Jay,[4] A. S. Kronfeld,[4,†] J. Laiho,[9] Ruizi Li,[1] Yin Lin,[10,4] P. B. Mackenzie,[4] A. S. Meyer,[11,‡] E. T. Neil,[12,13] J. Osborn,[14] J. Simone,[4] A. Strelchenko,[4] R. Sugar,[15] D. Toussaint,[16] and R. S. Van de Water[4]

(Fermilab Lattice and MILC Collaborations)

[1]*Michigan State University, East Lansing, Michigan, USA*
[2]*University of Utah, Salt Lake City, Utah, USA*
[3]*University of Illinois, Urbana, Illinois, USA*
[4]*Fermi National Accelerator Laboratory, Batavia, Illinois, USA*
[5]*Universidad de Granada, Granada, Spain*
[6]*Indiana University, Bloomington, Indiana, USA*
[7]*American Physical Society, Ridge, New York, USA*
[8]*University of Kentucky, Lexington, Kentucky, USA*
[9]*Syracuse University, Syracuse, New York, USA*
[10]*University of Chicago, Chicago, Illinois, USA*
[11]*Brookhaven National Laboratory, Upton, New York, USA*
[12]*University of Colorado, Boulder, Colorado, USA*
[13]*RIKEN-BNL Research Center, Upton, New York, USA*
[14]*Argonne National Laboratory, Argonne, Illinois, USA*
[15]*University of California, Santa Barbara, California, USA*
[16]*University of Arizona, Tucson, Arizona, USA*

(Dated: March 3, 2019)

Abstract

We propose to continue our computation of the axial-vector form factor of the nucleon using the highly-improved staggered-quark (HISQ) action for both valence and sea quarks. We use the (2+1+1)-flavor HISQ ensembles generated at the physical point, combining lattice QCD calculations of the q^2 dependence with the z expansion to obtain a model-independent description of the shape. As a by-product, we will compute the axial charge g_A directly at the physical point. We will test our approach with the shape of the vector form factor, which is constrained by high-statistics electron-scattering data. The project is well aligned with USQCD goals, because the axial-vector form factor is an important ingredient in quasielastic neutrino-nucleon scattering, which is the key signal process in neutrino-oscillation experiments at Fermilab.

We request 203 kGPU-hours and 3 M `Sky`-core-hours at BNL or Fermilab; we also request 50 Tbyte disk space and 108 Tbyte tape storage. If we continue running at BNL and the tape storage has to be at Fermilab or JLab, some scratch space for staging to the tape robot is also needed. Using USQCD conversion factors, the total request is 10 M `Sky`-core-hours.

* chughes@fnal.gov
† ask@fnal.gov
‡ ameyer@quark.phy.bnl.gov

I. INTRODUCTION

In 2014, the Particle Physics Project Prioritization Panel (P5) recommended a suite of short- and long-baseline neutrino experiments as the core of the coming, domestic, accelerator-based high-energy physics program [1]. The main motivations are to answer questions that explore beyond the Standard Model: What are the neutrino mass and oscillation parameters, including CP violation? Are neutrinos Majorana particles? Are there additional sterile species of neutrino? Do neutrinos interact in non-Standard ways, for example as they pass through matter? Since 2015, Fermilab and its partners have taken several steps toward answering these questions, with results from NOvA, MINERvA, and MicroBooNE, refurbishment of ICARUS at CERN and transport to Fermilab, and establishment of a strong international collaborations for the future long-baseline DUNE and short-baseline SBND experiments.

These questions sound remote from QCD, but the essence of the experimental technique is neutrino-nucleus scattering. Until recently, the goal has been to demonstrate that neutrino mixing parameters are nonzero, and neutrino-oscillation experiments (mostly) circumvented hadronic and nuclear physics with measurements of flux$\times$(cross section) from a near detector. Now that experiments are moving from first observations to precise measurements, the theoretical understanding of the neutrino-nucleus interaction will play an ever more important role.

Figure 1 depicts the interplay of nuclear physics, hadronic physics, and neutrino physics. The key signal process is charged-current quasielastic scattering, $\nu_l n \to l^- p$ (or $\bar{\nu}_l p \to l^+ n$), i.e., with no extra pions. As it stands (Fig. 1, left), scattering data must be analyzed assuming both a form-factor model for the nucleon-level transition and nuclear models. The latter describe the initial state of the nucleon inside the nucleus and also how final-state interactions with the nucleus modify the signal. For example, primary pions could be absorbed by the nucleus, or secondary pions could be created after the initial scatter. The experimental data are then studied further, often with a Monte Carlo such as GENIE [2], to look for self-consistency of the hadronic and nuclear models. Even when this process converges to a stable description of the data, it introduces an unquantifiable uncertainty into estimates of neutrino-oscillation parameters, θ_{ij} and δ_{CP}.

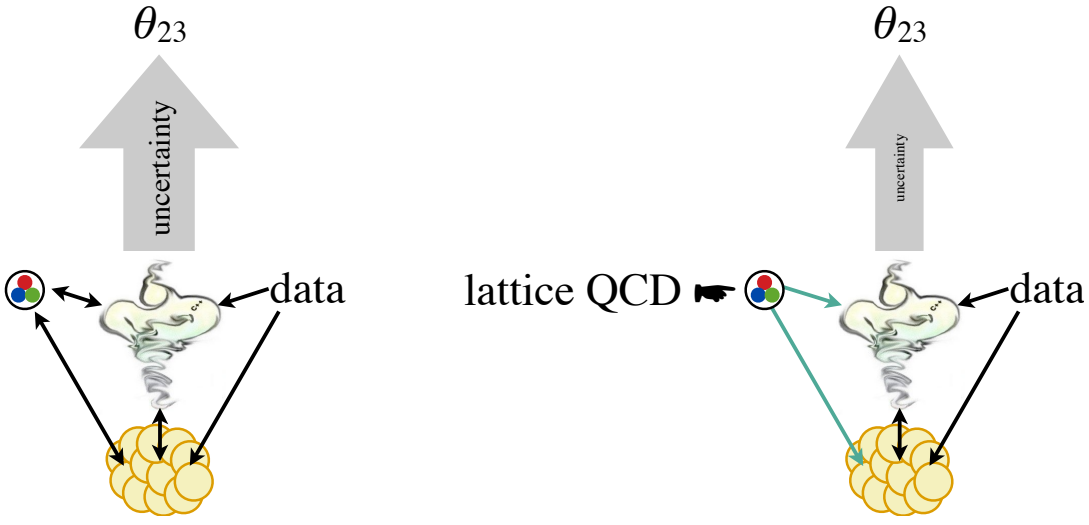

FIG. 1. Left: current interplay between data, hadronic physics (circle enclosing a red, green, and blue quark), and nuclear physics (collection of nucleons at the bottom), feeding into the GENIE Monte Carlo [2] and ultimately uncertainties on oscillation parameters, such as θ_{23}. Right: sketch of the disruption possible with *ab initio* calculations from lattice QCD.

The neutrino-nucleon interaction can be understood, from first principles, with lattice QCD. Nucleon physics is a challenge, so (for now) we address the obvious first step: a calculation of the shape of the axial-vector form factor. Calculations of this form factor have a considerable history in lattice QCD and have been found to be much more demanding than those of meson form factors. Some of the challenges are a difficult chiral extrapolation, large finite-volume effects, and contamination from excited states in lattice-QCD correlation functions. We address the first two problems with the HISQ ensembles [3, 4]. We propose to start with the physical-point ensembles, so no chiral extrapolation will be needed. The physical volumes of these ensembles are large: $L > 5$ fm, $3.3 \leq M_\pi L \leq 3.9$. Thus, finite-volume effects should be under control.

II. METHODS

Neutrino-nucleon scattering is mediated by W-boson exchange. In quasielastic scattering, we are interested in the matrix elements

$$\langle p(\boldsymbol{p})|\mathscr{V}_\mu^+|n(\boldsymbol{k})\rangle = \bar{u}_p(\boldsymbol{p})\left[\gamma_\mu F_1(q^2) + \frac{i\sigma_{\mu\nu}q^\nu}{2M_N}F_2(q^2)\right]u_n(\boldsymbol{k}), \tag{2.1}$$

$$\langle p(\boldsymbol{p})|\mathscr{A}_\mu^+|n(\boldsymbol{k})\rangle = \bar{u}_p(\boldsymbol{p})\left[\left(\gamma_\mu - \frac{2M_N q_\mu}{q^2}\right)\gamma^5 F_A(q^2) + \frac{2M_N q_\mu}{q^2}\gamma^5 F_P(q^2)\right]u_n(\boldsymbol{k}), \tag{2.2}$$

where $\bar{u}_p$ and u_n are nucleon spinor wave functions, $\mathscr{V}_\mu^+$ and $\mathscr{A}_\mu^+$ are the (continuum) charged vector and axial-vector currents, M_N is the nucleon mass (neglecting isospin), and $q = p - k$ is the momentum transfer. Neutrino physics needs the axial form factor $F_A(q^2)$, while the vector form factor $F_1(q^2)$ can be used to build confidence in our results, because its shape is constrained (up to radiative corrections and isospin violation) by high-statistics electron-nucleon scattering. In neutrino scattering, the form factors F_2 and F_P are not as important as F_1 and F_A.

A. Staggered Baryon Operators

Operators for baryons with staggered quarks have been studied in the past [5, 6]. In general, composite operators of staggered fields with good quantum numbers are spread over a 2^3-site cube on a timeslice t. One introduces

$$\psi_{iA}^a(y) = \chi_i^a(y + A), \tag{2.3}$$

where χ is the one-component field in the staggered action (of color a and flavor i). The coordinate y labels the origin of the cubes (and $y_4 = t$), and A is a sum of unit vectors connecting y to the other corners of the spatial cube. One then introduces a basic trilinear [5, 6]

$${}_{ijk}\mathscr{B}_{ABC}(y) = \varepsilon^{abc}\psi_{iA}^a(y)\psi_{jB}^b(y)\psi_{kC}^c(y) \tag{2.4}$$

that has been antisymmetrized over color. Gauge symmetry can be enforced by inserting gauge links on a path from $y + A$ back to y or, for A consisting of 2 or 3 directions, an average over various paths. We use Coulomb gauge for corner wall sources (see below), which inserts implicit averages over many paths.

Generic baryon two-point and three-point correlators are then

$${}_{ijk\bar{i}\bar{j}\bar{k}}C_{ABC\bar{A}\bar{B}\bar{C}}(t) = \frac{1}{N_s^3}\sum_{\boldsymbol{y}}\langle {}_{ijk}\mathscr{B}_{ABC}(y)\ {}_{\bar{i}\bar{j}\bar{k}}\bar{\mathscr{B}}_{\bar{A}\bar{B}\bar{C}}(z)\rangle, \tag{2.5}$$

$$ {}_{ijk\bar{i}\bar{j}\bar{k}}C^{\mu}_{ABC\bar{A}\bar{B}\bar{C}}(t,\tau) = \frac{1}{N_s^6}\sum_{\boldsymbol{x},\boldsymbol{y}} e^{i\boldsymbol{p}\cdot(\boldsymbol{x}-\boldsymbol{y})} \langle {}_{ijk}\mathscr{B}_{ABC}(y)\, A^{\mu}(x)\, {}_{\bar{i}\bar{j}\bar{k}}\bar{\mathscr{B}}_{\bar{A}\bar{B}\bar{C}}(z)\rangle, \tag{2.6} $$

with N_s^3 lattices, Euclidean times $x_4 = \tau$, $y_4 = t$, and origin (for now) $z = 0$. The lattice axial current, $A^{\mu}(x)$, is a bilinear of the staggered-fermion field. $\bar{\mathscr{B}}$ is constructed by replacing quark fields in Eq. (2.4) with antiquark fields. In practice, the $\mathscr{B}$ and $\bar{\mathscr{B}}$ operators are contracted with coefficient tensors ${}^{ijk}\mathscr{O}_r^{RABC}$ and ${}^{\bar{i}\bar{j}\bar{k}}\bar{\mathscr{O}}_{\bar{r}}^{\bar{R}\bar{A}\bar{B}\bar{C}}$, where r and $\bar{r}$ label the irreducible representation (irrep) of the staggered-fermion symmetry group, and R and $\bar{R}$ label the component within the irrep. Below, we refer to sums over (A,B,C) and $(\bar{A},\bar{B},\bar{C})$ as "tie-ups." As discussed in Sec. II B, the construction of Ref. [6] yields several operators for each irrep r.

As discussed in previous proposals, we start with the corner-wall source [7–10], solving

$$ (D+m)^{ac}_{AC} G^{cb}_{CB}(y,z_4) = \delta^{ab}\delta_{y_4,z_4}\sum_{\boldsymbol{z}} \delta_{\boldsymbol{y}+\boldsymbol{A},\boldsymbol{z}+\boldsymbol{B}}, \tag{2.7} $$

where, as above, $\boldsymbol{y}$ (y) and $\boldsymbol{z}$ (z) denote the coordinates of (hyper)cubes, and A, B, C the location within spatial cubes. Here, a and b are color indices. These propagators play a key role, and the previous two allocation years' propagators are stored on tape,[1] so we can continue to use them.

For the current insertion, we adopt two different strategies, both of which use a sequential propagator from the current for the daughter quark in the three-point function. The first strategy, which we call the corner current, puts the local current at a single corner, $\boldsymbol{D}$, of the unit cube, solving

$$ (D+m)^{ac}_{AC}\widehat{G}^{cb}_{CB;\boldsymbol{q},D}(x,y_4,z_4) = \delta^{ab}\delta_{x_4,y_4}\sum_{\boldsymbol{y}} \delta_{\boldsymbol{x}+\boldsymbol{A},\boldsymbol{y}+\boldsymbol{D}} e^{-i\boldsymbol{q}\cdot(\boldsymbol{y}+\boldsymbol{D})}\, G^{cb}_{DB}(y,z_4), \tag{2.8} $$

for momentum transfer $\boldsymbol{q}$, where the parent propagator $G^{cb}_{DB}(y,z_4)$ is computed from Eq. (2.7). In practice, we choose the corner for the current insertion at random from one configuration to the next. The different choices of $\boldsymbol{D}$ are later summed with correct choice of staggered and Fourier phases when performing the ensemble average; we have used it for the zero-momentum vector current, i.e., g_V (ideally = 1). This method has the advantage of flexibility, because all spin-taste currents are accessible. Moreover, it is possible to come back later and fill in the missing corners to improve statistics. Once propagators from all eight corners have been computed, this approach yields information equivalent the our second strategy.

The second strategy, which we call a spin-taste current, explicitly projects the desired spin-taste quantum numbers at the current insertion. This strategy provides an extra factor of 8 statistics in the volume average over the corner-only current of Eq. (2.8) for the same computational cost due to the sum over corners, but restricts the spin-taste of the current insertion. In practice, we do inversions for only the spin-taste current $A_3\otimes A_3$, which is obtained by applying a relative phase of -1 to sites an odd number of sites away from the origin in the z direction. This current insertion may be obtained by solving the equation

$$ (D+m)^{ac}_{AC}\widetilde{G}^{cb}_{CB;\boldsymbol{q},A_3\otimes A_3}(x,y_4,z_4) = \delta^{ab}\delta_{x_4,y_4}\sum_{\boldsymbol{D},\boldsymbol{y}} \delta_{\boldsymbol{x}+\boldsymbol{A},\boldsymbol{y}+\boldsymbol{D}} e^{-i\boldsymbol{q}\cdot(\boldsymbol{y}+\boldsymbol{D})}(-1)^{\boldsymbol{D}_3}\, G^{cb}_{DB}(y,z_4). \tag{2.9} $$

Similarly, the local $V_4\otimes V_4$ vector current requires a daughter propagator with $(-1)^{\boldsymbol{D}_3}$ replaced by $(-1)^{\boldsymbol{D}_1+\boldsymbol{D}_2+\boldsymbol{D}_3}$, and so on for other currents. This strategy is more cost effective when a

[1] A few from the smallest lattices have been lost but are cheap to recompute.

TABLE I. Zero-momentum fermionic irreps of GTS $\times$ $\mathrm{SU}_{\mathrm{isospin}}(2)$ [6]. Colloquially, the different N-like and Δ-like states in each irrep can be called "tastes."

GTS | isospin:	$\frac{3}{2}$	$\frac{1}{2}$
8	$3N$, 2Δ	$5N$, 1Δ
$8'$	$0N$, 2Δ	$0N$, 1Δ
16	$1N$, 3Δ	$3N$, 4Δ

small subset of spin-taste combinations are needed; we have used it for the zero-momentum axial current, i.e, g_A.

A general three-point function can be computed by starting the inversion at $z_4 = 0$ and N_{sep} values of the source-to-insertion time separation, $y_4 - z_4$. An inversion is required for each of N_{mom} choices of momentum and N_{cur} choices of spin-taste– or corner-current insertions. This setup requires

$$N_{\mathrm{inv}} = 8N_c \left(1 + N_{\mathrm{mom}} N_{\mathrm{cur}} N_{\mathrm{sep}}\right) \tag{2.10}$$

runs of the (single-color) inverter per configuration, where $N_c = 3$ is the number of colors. Our current plan for the axial charge (and vector charge as a cross check) is to proceed with $N_{\mathrm{mom}} = 1$, $N_{\mathrm{cur}} = 2$, and $N_{\mathrm{sep}} = 4$. For nonzero momentum, we will include an additional $N_{\mathrm{mom}} = 3$ momenta with $N_{\mathrm{sep}} = 4$ and $N_{\mathrm{cur}} = 1$ for a (randomly chosen) corner current only. With additional effective run time (through better hardware, better inverters, or opportunistic running) we will fill in the missing corners, as long as the additional statistics are helpful. As is common in nucleon and B physics, we can also repeat the calculations (beyond this proposal) for several choices for the initial time z_4.

B. Excited States

To discuss our strategy for excited states, it is useful to recall some aspects of the group theory for two or three flavors of staggered fermions [6]. The eight quark fields ψ_A on a spatial cube transform as an 8 under the geometrical timeslice group of staggered fermions (GTS) [5, 6]. The u and d flavors form an isodoublet as always. Baryons thus transform under the tensor product $(8, \frac{1}{2}) \otimes (8, \frac{1}{2}) \otimes (8, \frac{1}{2})$, which can be reduced into a direct sum of irreps, as shown in Table I. The $I = \frac{3}{2}$ ($I = \frac{1}{2}$) column stems from fully symmetric (mixed symmetry) irreps with respect to isospin. Let us refer to states that yield the nucleon (Δ) mass in the continuum limit as "N-like" ("Δ-like"). Operators in the irreps $(8, \frac{3}{2})$, $(8, \frac{1}{2})$, $(16, \frac{3}{2})$, and $(16, \frac{1}{2})$ couple to both N-like and Δ-like baryons and, as usual with staggered fermions, parity partners. These four irreps can be used for both three- and two-point functions. Owing to the taste quantum number, N-like states need not have isospin $\frac{1}{2}$ [6]. Operators in the irreps $(8', \frac{3}{2})$ and $(8', \frac{1}{2})$ couple to Δ-like but not N-like states.

The entries in Table I often list more than one taste and kind of state. A useful feature of the construction in Ref. [6] is that several operators arise in each irrep. They differ in the way the quark fields are spread out over the cube. Moreover, the number of operators coincides with the number of distinct baryons in each entry of Table I. For example, in the $(16, \frac{3}{2})$ irrep, we have four baryon operators and, thus, compute a 4×4 matrix correlator. This feature holds throughout Table I. We have found, however, that it can be impossible to disentangle all tastes if the statistical uncertainties are not smaller than the size of the taste splittings [11].

C. Normalized Axial-Vector Current

To project out the pseudoscalar form factor, let us define

$$A_\perp^\mu = A^\mu - \frac{q^\mu}{q^2} q \cdot A. \tag{2.11}$$

Then, for $q \neq 0$,

$$\langle p(\boldsymbol{p}) | Z_A A_\perp^\mu | n(\boldsymbol{k}) \rangle = \bar{u}_p(\boldsymbol{p}) \gamma_\perp^\mu \gamma^5 u_n(\boldsymbol{k}) F_A(q^2), \tag{2.12}$$

where A^μ is the local or one-link lattice current, and Z_A is its matching factor, such that $Z_A A^\mu$ and the continuum current $\mathscr{A}^\mu$ have the same matrix elements.

We can eliminate the matching factor Z_A via ratios. In the case of the axial-vector current, we will form the combination

$$F_A(q^2) \bar{u}_p(\boldsymbol{p}) \gamma_\perp^\mu \gamma^5 u_n(\boldsymbol{k}) = \left. \frac{\langle p(\boldsymbol{p}) | Z_A A_\perp^\mu | n(\boldsymbol{k}) \rangle}{\langle 0 | Z_A A^4 | \pi(\boldsymbol{0}) \rangle \, \omega^2} \right|_{\text{this work}} \left. \frac{\langle 0 | 2\hat{m} P | \pi \rangle}{M_\pi} \right|_{\text{Ref. [12]}} \omega^2 \big|_{a \to 0}, \tag{2.13}$$

where P in the second factor is the absolutely normalized pseudoscalar density (with pseudoscalar taste), and ω is a relative scale-setting distance. The factor Z_A cancels. The pion decay constant from A^μ, $\langle 0 | Z_A A^\mu | \pi(\boldsymbol{0}) \rangle$, will be calculated as part of this project. The second factor comes from our project on light decay constants [4, 12], as does f_{p4s} (a good choice for $1/\omega$). MILC has also published results for the gradient-flow lengths $\sqrt{t_0}$ and w_0 on the HISQ ensembles [13]. Uncertainties in the second and third factors will be subdominant, because they do not entail nucleons. We will use Eq. (2.13) both for g_A, with $\boldsymbol{p} = \boldsymbol{k} = \boldsymbol{0}$, and for the shape, with $\boldsymbol{p} \neq \boldsymbol{0}$.

D. Methodology for Form-Factor Shapes

In the past, a dipole parametrization has been used to fit experimental data and, also, lattice-QCD data:

$$F_A(q^2) = -g_A \left(1 - q^2/M_A^2\right)^{-2}. \tag{2.14}$$

Although a q^{-4} fall-off can be justified for asymptotically high q^2, this form is inconsistent with QCD in the region of interest. It is also inadequate to describe electron-nucleon scattering data for $F_1(q^2)$ [14, 15]. The value at $q^2 = 0$ is well-known from neutron beta decay, $g_A = 1.2724(23)$ [16].

As neutrino scattering data have become more precise and the range of q^2 probed more diverse, different results for M_A have been reported. Among recent experiments, the NOMAD Collaboration [17] reports $M_A = 1.05 \pm 0.02 \pm 0.06$ GeV, while the MiniBooNE Collaboration [18] reports $M_A = 1.35 \pm 0.17$ GeV. These error bars do not reflect defects in the dipole parametrization.

Bhattacharya, Hill, and Paz [19] have proposed using a parametrization based on analyticity and unitarity. In the complex $t = q^2$ plane, $F_A(t)$ has a cut on the real axis for $t > t_{\text{cut}} \equiv 9M_\pi^2$ and is analytic elsewhere. One can map the q^2 plane onto the unit disk via

$$z(t, t_{\text{cut}}, t_0) = \frac{\sqrt{t_{\text{cut}} - t} - \sqrt{t_{\text{cut}} - t_0}}{\sqrt{t_{\text{cut}} - t} + \sqrt{t_{\text{cut}} - t_0}}, \tag{2.15}$$

where t_0 can be chosen for convenience. This change of variables maps the cut to the unit circle; the small region for beta decay, $m_e^2 \leq t \leq (M_n - M_p)^2$, is mapped to a short interval of real z; the

scattering region $t < 0$ is mapped to another interval, which extends to $z \to 1$ as $t \to -\infty$. See Fig. 4 in the appendix for an illustration. The endpoints of these intervals depend on t_0.

Analyticity implies that the form factor can be expanded as a power series in z,

$$F_A(q^2) = \sum_{k=0}^{\infty} a_k z(q^2, t_{\rm cut}, t_0)^k, \tag{2.16}$$

and unitarity places a bound on the coefficients a_k, such that the expansion converges for $|z| < 1$. If an experiment or a lattice-QCD calculation accesses the range $-Q^2_{\rm max} \le q^2 \le 0$, then choosing

$$t_0 = t_{\rm cut}\left(1 - \sqrt{1 + Q^2_{\rm max}/t_{\rm cut}}\right), \tag{2.17}$$

minimizes $|z|$. For example, typical experiments reach $Q^2_{\rm max} \approx 1.0$ GeV^2, for which case $|z| \le 0.24$, so quadratic and higher terms are naturally very small. Recently, this formalism has been applied to old bubble-chamber data for neutrino-deuteron scattering [20].

Following a successful procedure used by the Fermilab Lattice and MILC Collaborations in B physics [21–23], we will fit the lattice data to the z expansion. We plan to use the rest frame for the neutron, $\boldsymbol{k} = \boldsymbol{0}$, placed at the source in the discussion of Sec. II A. In this frame, the scattered proton should reach momenta up to $|\boldsymbol{p}|_{\rm max} = \sqrt{Q^2_{\rm max}} = 0.7$ GeV. The box sizes of the HISQ ensembles lead to the quantum of momentum $2\pi/L = 0.21$–0.25 GeV.

Therefore, it seems sufficient to use $\boldsymbol{p} = \boldsymbol{0}$, $2\pi(1,0,0)/L$, and $2\pi(1,1,0)/L$. We will study whether we retain a signal at $2\pi(1,1,1)/L$. If not, we will use twisted boundary conditions in order to access arbitrary values of momentum to reach the maximum Q^2 that still gives a signal. The output of the fit will be the first two or three coefficients a_k in Eq. (2.16), together with their errors and correlation matrix.

E. Blind Analysis of g_A

Our calculation of the normalization, g_A, is being done with a blinding factor. In our B- and D-physics calculations, we introduced blinding via a small but significant multiplicative offset in the perturbative matching factor. Here that simple scheme is not available. Instead, the three-point code multiplies all nucleon three-point data with an offset before writing out the file. The offset is known to no one, and only a few collaborators have the key needed to reveal it.

F. Related Calculations by Other Groups

Several collaborations around the world are pursuing calculations of nucleon form factors, including g_A. As mentioned above, most other efforts have box-size $L < 3$ fm for most, if not all, of the ensembles. In 2015, the European Twisted Mass collaboration published a result for g_A (and other zero-momentum matrix elements) at physical quark mass, albeit with $n_f = 2$ and only one lattice spacing [24]; the physical mass ensemble has $M_\pi L = 3$. The Mainz group [25] is extending its work on vector form factors to the axial current, using the CLS ensembles with $n_f = 2$ and (so far) $a \approx 0.05$ fm, $M_\pi \approx 332$ MeV, $M_\pi L = 4.0$. In the past year, JLQCD [26] released a result on four ensembles with different pion masses ranging from $290 - 540$ MeV and $M_\pi L \approx 3.9 - 5.1$; Bali *et al.* [28] have results for ten ensembles for $M_\pi L \approx 3.4$–6.7 and pion masses down to 150 MeV; and Egerer *et al.* [29] have results for a single ensemble at $M_\pi \approx 350$ MeV using

distillation to control for excited states. Moreover, PACS [30] has computed the axial form factor on a single ensemble at $M_\pi \approx 146$ MeV with $M_\pi L \approx 6.0$. Within USQCD, there are efforts on clover ensembles [31] and on domain-wall ensembles (1 so far) [27]. The PNDME Collaboration is pursuing calculations of nucleon matrix elements on the HISQ ensembles, including g_A and form factors. They simulate valence quarks with the clover action, however. They have published results based on the nine HISQ ensembles with $a \approx 0.06$, 0.09, and 0.12 fm [33, 34]. (At $a \approx 0.12$ fm, PNDME used the middle volume.) Similarly, the CalLat Collaboration uses domain-wall fermions on the HISQ ensembles to obtain a precise value of g_A [35]. Given the importance of these topics to both high-energy and nuclear physics, it is important, we believe, to have cross-checks and to make full use of the investments made in the HISQ ensembles.

III. CODE AND ITS READINESS

We use the MILC code base [36], which is well known within USQCD. At the beginning of this project, we extended the MILC code base to two- and three-point functions with the operators discussed in Sec. II A, and in the 2017-18 allocation year we wrote the modifications needed for sequential propagators. Consequently, both the GPU code for computing inversions and the *threaded* CPU code for tie-ups of correlation functions are in production. Nonzero momenta on the $a \approx 0.15$ fm ensemble will be computed without twisted boundary conditions: this code is in place. On the other ensembles, nonzero momenta will be computed with twisted boundary conditions to give the same physical momentum as on the $a \approx 0.15$ fm ensemble; this code requires only modest modifications to the existing tie-up code, so it does not pose an obstacle. In the 2018-19 allocation year we ported our operations from Fermilab to BNL. The run plan in Sec. IV B will continue seamlessly from our current running. Note that staggered inverters on Skylake architecture cost twice as much as on `pi0`, so we have focused our inversions on the BNL IC.

We continue to look for ways to optimize. One of us belongs to the exascale algorithm development group, working on implementation of a number of efficient fermion inverters for QUDA library, such as the block-CG [37]. The developer group is also focused on optimization of the multigrid algorithm for the staggered operator [38], which is based on the existing QUDA multigrid framework [39]. Of course, none of these developments will be moved into our production code until they are certified. We raise the point simply to emphasize that our running has the potential to improve over the course of the year.

IV. RESOURCES

A. Timings and Resources Requested

Tables II–V summarize the time needed for separate components of the computation: two- and three-point correlators at zero and nonzero momentum. Table VI gathers the total for the four components. From a computing perspective, the project naturally falls into four parts: two-point functions at zero momentum (inversions and tie-ups; Table II); three-point functions at zero momentum (inversions and tie-ups; Table III); two-point functions at nonzero momentum (tie-ups only; Table IV); three-point functions at nonzero momentum (inversions and tie-ups; Table V).

B. Quarterly Run Plan

In the tables, the right-most columns spell out our run plan needed to achieve four physics milestones. From our previous allocations, shown in Table II, we have already generated the two-point data at three lattice spacings and have computed the nucleon mass (first milestone; a paper is due to be submitted soon). In the first quarter (Q1), we aim to finish the full nonzero-momentum three-point running at $a \approx 0.15$ fm (Table V), which will demonstrate that we can compute form factors' q^2 dependence (second milestone). We will then write a paper documenting the demonstration, which will be used to support applications to other sources of computing for the $a \approx 0.06$ fm physical-mass ensemble.

TABLE II. Timings on `pi0` and `pi0g` needed to generate the HISQ zero-momentum two-point correlators on the physical-mass ensembles. These inversions account for the "1" in Eq. (2.10), i.e., 24 single-color inversions per configuration. We define kGPU = 1000 K80-GPU-hours and M`Sky` = 10^6 `Sky`-core-hours.

$\approx a$ (fm)	$N_s^3 \times N_t$	N_{meas}	N_{left}	Inversions	2-pt tie-ups M`Sky`	Status	When
0.15	$32^3 \times 48$	3000		0.10 M`Sky`	0.004	Done	AY 2016–17
0.15	$32^3 \times 48$	3500	0	0.11 M`Sky`	0.004	Done	AY 2016–18
0.12	$48^3 \times 64$	1000	0	0.20 M`Sky`	0.006	Done	AY 2017–18
0.09	$64^3 \times 96$	1047	0	13.33 kGPU	0.137	Done	AY 2017–19

TABLE III. Timings on `pi0` and `pi0g` needed to generate the HISQ zero-momentum three-point correlators on the physical-mass ensembles. Here $N_{\text{mom}} = 1$, $N_{\text{cur}} = 2$, and $N_{\text{sep}} = 4$, leading to 192 single-color inversions. These timing estimates assume that all propagators from the zero-momentum 2-pt calculation have been saved to tape.

$\approx a$ (fm)	$N_s^3 \times N_t$	N_{meas}	N_{left}	Inversions	3-pt tie-ups M`Sky`	Status	When	
0.15	$32^3 \times 48$	3500	0	0.89 M`Sky`	0.12	Done	AY 2017–18	
0.12	$48^3 \times 64$	1000	0	29.09 kGPU	0.14	Done	AY 2018–19	
0.09	$64^3 \times 96$	1047	1047	106.60 kGPU	0.54	Proposed	AY 2019–20	Q2, Q3
Total $= \sum \text{time} \cdot N_{\text{left}}/N_{\text{meas}}$				**106.60 kGPU**	**0.80**	Proposed	AY 2019–20	

TABLE IV. Timings on `pi0` and `pi0g` needed to generate $N_{\text{mom}} = 3$ HISQ nonzero momentum two-point correlators on the physical-mass ensembles. These timing estimates assume that all propagators from the zero-momentum two-point calculation have been saved to tape. Note that we retain some propagators with last year's random-wall sources for $a \approx 0.15$ fm and 0.12 fm. Storage in *italics* for clarity.

$\approx a$ (fm)	$N_s^3 \times N_t$	N_{meas}	Inversions Tbyte	2-pt tie-ups M`Sky`	Status	When	
0.15	$32^3 \times 48$	3500	*34.30*	0.01	Done	AY 2018–19	
0.12	$48^3 \times 64$	1000	*44.00*	0.02	Proposed	AY 2019–20	Q1
0.09	$64^3 \times 96$	1047	*29.32*	0.06	Proposed	AY 2019–20	Q2
Total			***107.62***	**0.09**	Proposed	AY 2019–20	

TABLE V. Timings on `pi0` and `pi0g` needed to generate the HISQ nonzero momentum three-point correlators on the physical-mass ensembles. For this table, we take $N_{\rm mom} = 3$, $N_{\rm cur} = 1$, and $N_{\rm sep} = 4$, leading to 288 single-color inversions. These timing estimates assume that all propagators from the zero-momentum 2-pt calculation have been saved to tape. Note that the total timing accounts for us already having generated a single non-zero momentum $a \approx 0.15$fm ensemble.

$\approx a$ (fm)	$N_s^3 \times N_t$	$N_{\rm meas}$	Inversions kGPU	3-pt tie-ups MSky	Status	When	
0.15	$32^3 \times 48$	3500	31.88	0.32	Proposed	AY 2019–20	Q1
0.12	$48^3 \times 64$	1000	43.64	0.37	Proposed	AY 2019–20	Q1
0.09	$64^3 \times 96$	1047	159.90	1.41	Proposed	AY 2019–20	Q3, Q4
Total			**224.79**	**2.10**	Proposed	AY 2019–20	

TABLE VI. Summary and total allocations. Here we define kGPU= 1000 K80-GPU-hours and MSky = 10^6 Sky-core-hours from running on `pi0g` and `pi0`. These timing estimates assume that all propagators from the zero-momentum 2-pt calculation have been saved to tape.

Component	Breakdown	Inversions all tie-ups kGPU	MSky	Tape storage Tbyte
2-pt ($\boldsymbol{p} = \boldsymbol{0}$)	Table II	0.00	0.00	–
3-pt ($\boldsymbol{p} = \boldsymbol{0}$)	Table III	106.60	0.80	–
2-pt ($\boldsymbol{p} \neq \boldsymbol{0}$)	Table IV	0.00	0.09	107.62
3-pt ($\boldsymbol{p} \neq \boldsymbol{0}$)	Table V	224.79	2.10	–
Total		**331.39**	**2.99**	**0.14** MSky
Remaining in AY 2018–19		128.50	0.0	
Request		**202.89**	**2.99**	**0.14** MSky

Concurrently in Q1, we will also generate the nonzero-momentum two- and three- point data at $a \approx 0.12$ fm (Tables IV and V). To evenly distribute our allocation time, in Q2, we will generate the majority of the zero-momentum $a \approx 0.09$ fm three-point data (Table III). We will also generate the nonzero-momentum two-point data at $a \approx 0.09$ fm (Table IV) to prepare for the nonzero-momentum three-point data at $a \approx 0.09$ fm (Table V) in Q3.

In Q3 we will finish the zero-momentum $a \approx 0.09$ fm three-point functions and have enough data to compute g_A at three lattice spacings (third milestone). The bulk of our allocation time is consumed by the $a \approx 0.09$ fm ensemble, and Q4 is solely dedicated to finishing the nonzero-momentum three-point functions on this ensemble. We will then have enough data to document the form-factor calculation at three lattice spacings (fourth milestone).

We have already generated all the data that needs to be kept for this project. Table IV outlines our storage needs. Here, we have the $a \approx 0.15$ fm and $a \approx 0.12$ fm propagators on tape at Fermilab (78TBs). However the $a \approx 0.09$ fm propagators are on disk (29TBs), split evenly between Fermilab and BNL. We would like to move these to tape storage. Our data management plan (attached as separate pdf) has been generated using dmptool.org, and exists for the duration of this project.

C. Human Resources

This project constitutes the heart of Yin Lin's Ph. D. research at the University of Chicago. Alexei Strelchenko of the Fermilab Scientific Computing Division is our link to algorithm development.

D. Resources Requested

In total, we request 203 kGPU-hours and 3 M `Sky`-core-hours to continue running at BNL or Fermilab; we also request 50 Tbyte disk space and 108 Tbyte tape storage. If we continue running at BNL and the tape storage has to be at Fermilab, some scratch space at Fermilab for staging is also needed. Using USQCD conversion factors, the total request is 10 M `Sky`-core-hours, at BNL or Fermilab.

With the tape back-up, we and other USQCD groups can use these data for other calculations. We ask that interested groups contact us to see whether the topics are of mutual interest.

V. RESULTS FROM 2015–2019

In the early stages, we obtained a blinded value of the axial charge, $\beta g_A = 1.45 \pm 0.22$ [40, 41], from 4000 configurations at $a \approx 0.15$ fm. The error here is statistical and from one ensemble only, preventing a thorough study of systematics.

We now have the nucleon mass on three lattice spacings, demonstrating feasibility of the all-staggered approach to nucleons. The results are shown in Fig. 2. Here we have studied both the generalized eigenvalue problem (GEVP) and a multi-exponential fit with Bayesian priors on excited states. This work has given us experience with fitting methodologies that will increase the throughput of the axial form factor work.

We also have three-point correlators with small statistical uncertainties. Figure 3 shows a (blinded) zero-momentum correlator with four source-current separations, both in raw form and scaled by the fit to the two-point functions. Here we have 3400 measurements on the $a \approx 0.15$ fm ensemble, yielding uncertainties of order of a few percent.

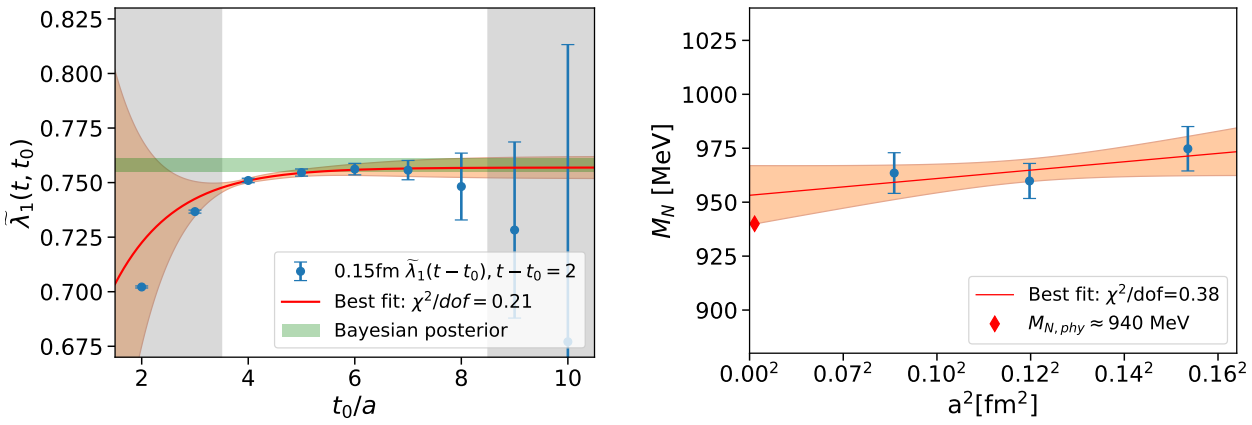

FIG. 2. Left: nucleon-mass results on the $a \approx 0.15$ fm ensemble. The blue points are lattice data, the orange curve is the fit function from the GEVP, and the green band is the Bayesian posterior. Right: Nucleon mass M_N vs. a^2 at three lattice spacings with our extrapolation. From paper in preparation.

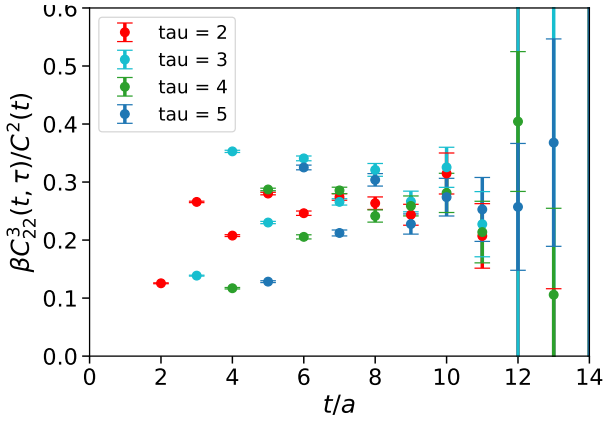

FIG. 3. Ratio of blinded three- and two-point correlators at various source-current insertion time, τ, on the $a \approx 0.15$ fm ensemble. Class-two operators are at the source and sink. The full matrix of two- and three-point correlators is shown in Appendix A.

VI. OUTLOOK

Eventually, we want to analyze all available physical-mass HISQ ensembles with $a \geq 0.06$ fm. Subsequently, we will examine other HISQ ensembles to carry out a finite-volume study at $a \approx 0.12$ fm and to connect our g_A with previous results at unphysical quark mass. In the longer term, other processes could be injected into Fig. 1, for example, $\nu n \to \ell^- \Delta^+$, nonresonant πp, and two-nucleon matrix elements of the form $\langle NN|A^\mu|NN\rangle$.

[1] S. Ritz *et al.*, "Report of the Particle Physics Project Prioritization Panel," (2014).

[2] "GENIE Neutrino Monte Carlo Generator," `http://www.genie-mc.org/`.

[3] A. Bazavov *et al.* (MILC), Phys. Rev. **D87**, 054505 (2013), arXiv:1212.4768 [hep-lat].

[4] A. Bazavov *et al.* (Fermilab Lattice, MILC), Phys. Rev. **D98**, 074512 (2018), arXiv:1712.09262 [hep-lat].

[5] M. F. L. Golterman and J. Smit, Nucl. Phys. **B255**, 328 (1985).

[6] J. A. Bailey, Phys. Rev. **D75**, 114505 (2007), arXiv:hep-lat/0611023 [hep-lat].

[7] C. W. Bernard *et al.*, Phys. Rev. **D48**, 4419 (1993), arXiv:hep-lat/9305023 [hep-lat].

[8] C. W. Bernard *et al.*, Phys. Rev. **D64**, 054506 (2001), arXiv:hep-lat/0104002 [hep-lat].

[9] H. Na, C. J. Monahan, C. T. H. Davies, R. Horgan, G. P. Lepage, and J. Shigemitsu (HPQCD), Phys. Rev. **D86**, 034506 (2012), arXiv:1202.4914 [hep-lat].

[10] A. Bazavov *et al.* (Fermilab Lattice, MILC), Phys. Rev. **D87**, 073012 (2013), arXiv:1212.4993 [hep-lat].

[11] Y. Lin (Fermilab Lattice), in *36th International Symposium on Lattice Field Theory (Lattice 2018)* (East Lansing, MI, United States, 2018).

[12] A. Bazavov *et al.* (Fermilab Lattice, MILC), Phys. Rev. **D90**, 074509 (2014), arXiv:1407.3772 [hep-lat].

[13] A. Bazavov *et al.* (MILC), Phys. Rev. **D93**, 094510 (2016), arXiv:1503.02769 [hep-lat].

[14] H. S. Budd, A. Bodek, and J. Arrington, (December, 2002), presented at the 2nd International Workshop on Neutrino-Nucleus Interactions in the Few GeV Region, arXiv:hep-ex/0308005 [hep-ex].

[15] J. C. Bernauer *et al.* (A1), Phys. Rev. **C90**, 015206 (2014), arXiv:1307.6227 [nucl-ex].
[16] M. Tanabashi *et al.* (Particle Data Group), Phys. Rev. **D98**, 030001 (2018).
[17] V. Lyubushkin *et al.* (NOMAD), Eur. Phys. J. **C63**, 355 (2009), arXiv:0812.4543 [hep-ex].
[18] A. Aguilar-Arevalo *et al.* (MiniBooNE), Phys. Rev. **D81**, 092005 (2010), arXiv:1002.2680 [hep-ex].
[19] B. Bhattacharya, R. J. Hill, and G. Paz, Phys. Rev. **D84**, 073006 (2011), arXiv:1108.0423 [hep-ph].
[20] A. S. Meyer, M. Betancourt, R. Gran, and R. J. Hill, Phys. Rev. **D93**, 113015 (2016), arXiv:1603.03048 [hep-ph].
[21] J. A. Bailey *et al.* (Fermilab Lattice, MILC), Phys. Rev. **D79**, 054507 (2009), arXiv:0811.3640 [hep-lat].
[22] J. A. Bailey *et al.* (Fermilab Lattice, MILC), Phys. Rev. **D92**, 034506 (2015), arXiv:1503.07237 [hep-lat].
[23] J. A. Bailey *et al.* (Fermilab Lattice, MILC), Phys. Rev. **D92**, 014024 (2015), arXiv:1503.07839 [hep-lat].
[24] A. Abdel-Rehim *et al.*, Phys. Rev. **D92**, 114513 (2015), (E) Phys. Rev. **D93**, 039904 (2016), arXiv:1507.04936 [hep-lat].
[25] S. Capitani, M. Della Morte, D. Djukanovic, G. M. von Hippel, J. Hua, B. Jäger, P. M. Junnarkar, H. B. Meyer, T. D. Rae, and H. Wittig, Int. J. Mod. Phys. **A34**, 1950009 (2019), arXiv:1705.06186 [hep-lat].
[26] N. Yamanaka, S. Hashimoto, T. Kaneko, and H. Ohki (JLQCD), Phys. Rev. **D98**, 054516 (2018), arXiv:1805.10507 [hep-lat].
[27] S. Ohta (LHP, RBC, UKQCD), in *36th International Symposium on Lattice Field Theory (Lattice 2018)* (East Lansing, MI, United States, 2018) arXiv:1810.09737 [hep-lat].
[28] G. S. Bali, S. Collins, M. Gruber, A. Schäfer, P. Wein, and T. Wurm, Phys. Lett. **B789**, 666 (2019), arXiv:1810.05569 [hep-lat].
[29] C. Egerer, D. Richards, and F. Winter, Phys. Rev. **D99**, 034506 (2019), arXiv:1810.09991 [hep-lat].
[30] K.-I. Ishikawa, Y. Kuramashi, S. Sasaki, N. Tsukamoto, A. Ukawa, and T. Yamazaki (PACS), Phys. Rev. **D98**, 074510 (2018), arXiv:1807.03974 [hep-lat].
[31] J. R. Green *et al.*, Phys. Lett. **B734**, 290 (2014), arXiv:1209.1687 [hep-lat].
[32] S. Ohta (RBC, UKQCD), PoS **LATTICE2014**, 149 (2015), arXiv:1410.8353 [hep-lat].
[33] T. Bhattacharya, V. Cirigliano, S. Cohen, R. Gupta, H.-W. Lin, and B. Yoon (PNDME), Phys. Rev. **D94**, 054508 (2016), arXiv:1606.07049 [hep-lat].
[34] R. Gupta, Y.-C. Jang, H.-W. Lin, B. Yoon, and T. Bhattacharya, Phys. Rev. **D96**, 114503 (2017), arXiv:1705.06834 [hep-lat].
[35] C. C. Chang *et al.*, Nature **558**, 91 (2018), arXiv:1805.12130 [hep-lat].
[36] MILC Collaboration, "MILC Code Version 7," (2016).
[37] M. A. Clark, A. Strelchenko, A. Vaquero, M. Wagner, and E. Weinberg, Comp. Phys. Comm. **233**, 29 (2018), arXiv:1710.09745 [hep-lat].
[38] R. C. Brower, M. A. Clark, A. Strelchenko, and E. Weinberg, Phys. Rev. **D97**, 114513 (2018), arXiv:1801.07823 [hep-lat].
[39] M. A. Clark, B. Joó, A. Strelchenko, M. Cheng, A. Gambhir, and R. Brower, (2016), arXiv:1612.07873 [hep-lat].
[40] A. S. Meyer, R. J. Hill, A. S. Kronfeld, R. Li, and J. N. Simone, PoS **LATTICE2016**, 179 (2017), arXiv:1610.04593 [hep-lat].
[41] A. S. Meyer, *The nucleon axial form factor and staggered lattice QCD*, Ph.D. thesis, University of Chicago (2017).

Appendix A: Extra figures

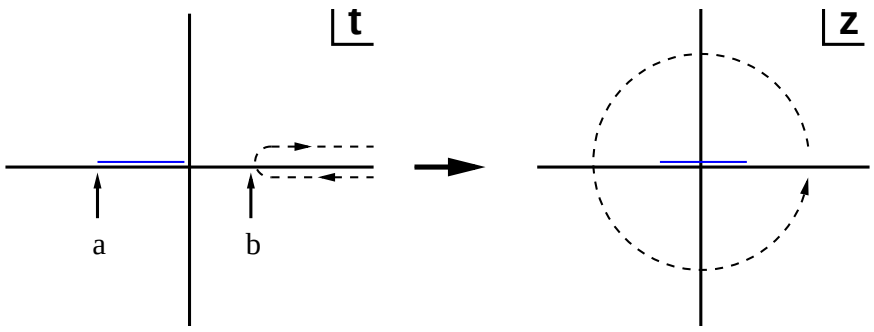

FIG. 4. The mapping of Eq. (2.15), which maps the whole complex t plane onto the unit disk in the complex z plane. The interval of real z for neutrino scattering is shown in blue. The point labeled "a" in the t plane corresponds to $-Q^2_{\rm max}$; "b" to $t_{\rm cut}$.

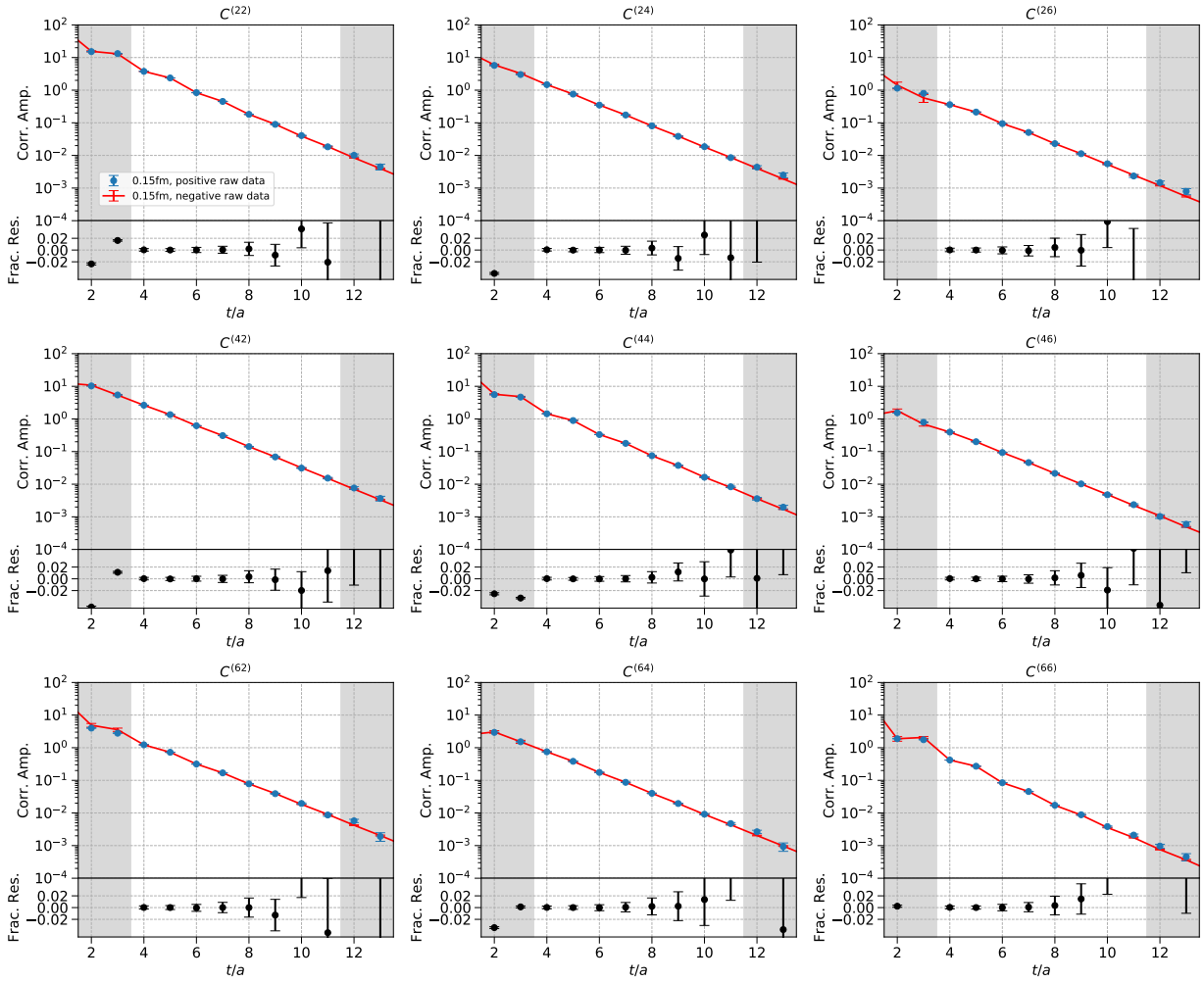

FIG. 5. Matrix of absolute value of two-point correlation functions in the $(16, \frac{3}{2})$ irrep on the $a \approx 0.15$ fm ensemble. The red curve is a fit using the Bayesian methodology. The fractional residue is the relative difference between the raw data and the fit result for the correlators.

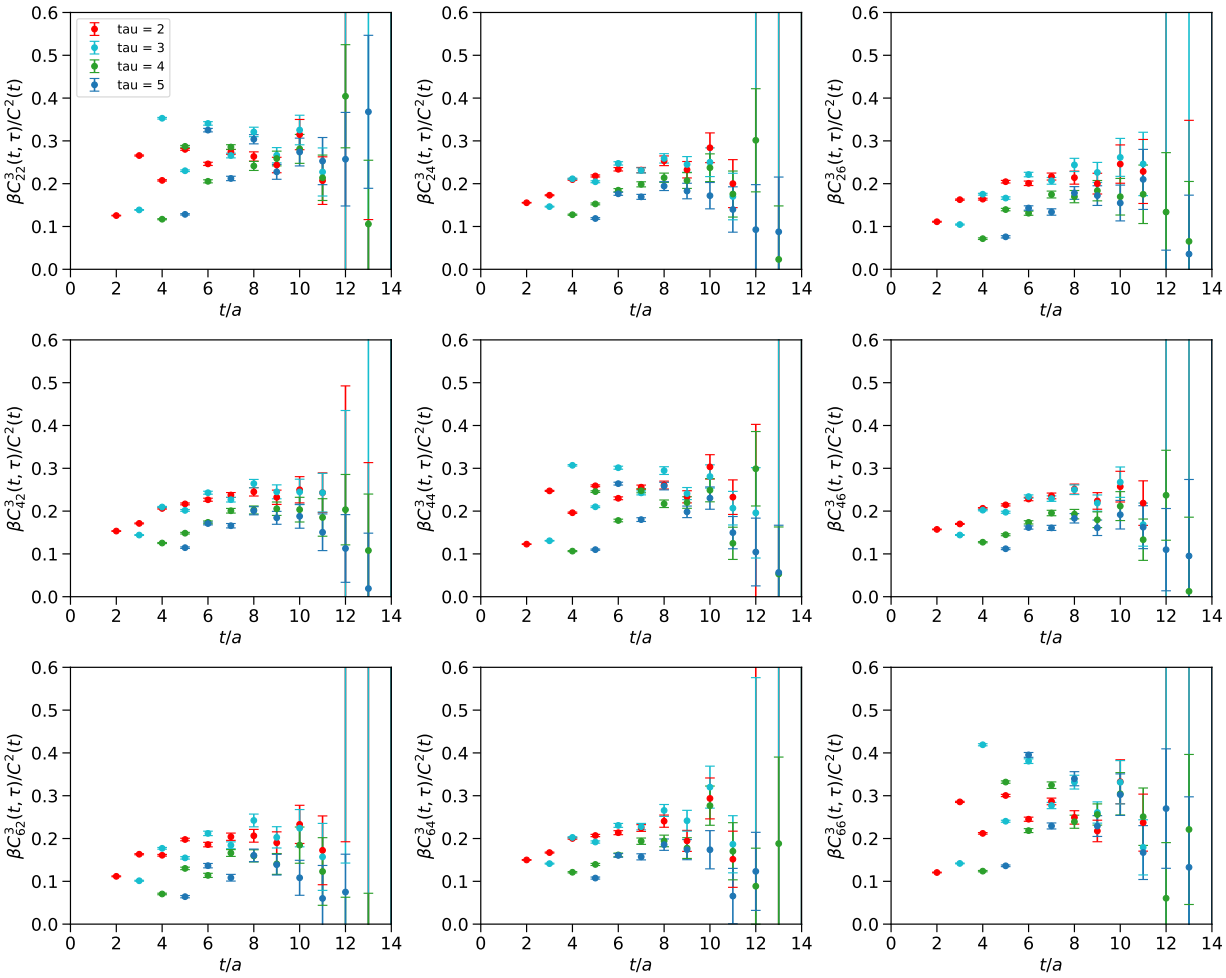

FIG. 6. Matrix of three-point correlation functions in the $(16, \frac{3}{2})$ irrep on the $a \approx 0.15$ fm ensemble. Here the ratio $\beta C^3_{ij}(t,\tau)/C^2$ is plotted, where β is the blinding factor (stored in a lock box but unknown). The four source-current separations are $\tau = 2$ (red), 3 (light blue), 4 (green), 5 (navy blue).